RSC Advances

PAPER

View Article Online
View Journal | View Issue

Check for updates

Cite this: *RSC Adv.*, 2018, **8**, 21879

D–A–D 2*H*-benzo[*d*][1,2,3]triazole derivatives as p-type semiconductors in organic field-effect transistors†

Iván Torres-Moya,*[a] Iratxe Arrechea-Marcos,[b] Carlos Tardío,[a] José R. Carrillo,[a] Ángel Díaz-Ortiz,[a] J. Teodomiro López Navarrete,[b] M. Carmen Ruiz Delgado,[b] Pilar Prieto*[a] and Rocío Ponce Ortiz*[b]

Received 16th April 2018
Accepted 30th May 2018

DOI: 10.1039/c8ra03246g

rsc.li/rsc-advances

A series of Donor–π–Acceptor–π–Donor compounds based on a 2*H*-benzo[*d*][1,2,3]triazole core branched with different alkynyl donor groups has been characterized and tested in organic field-effect transistors (OFETs). The electronic and molecular structures were elucidated through optical and vibrational spectroscopy in conjunction with DFT calculations. The results indicate that the planarity of the structure and the good intramolecular charge transfer from the electron-donating to the electron-withdrawing fragments play a critical role in the application of the compounds as semiconductors in OFET devices. The compounds were tested in a top-contact/bottom-gate thin film transistor architecture, and they behave as p-type semiconductors.

Open Access Article. Published on 13 June 2018. Downloaded on 12/9/2025 11:10:54 AM.
This article is licensed under a Creative Commons Attribution-NonCommercial 3.0 Unported Licence.

Introduction

Organic multifunctional semiconducting derivatives have attracted a great deal of attention in the last decade due to their potential applications in organic electronics, such as organic field-effect transistors (OFETs), organic solar cells, sensors, photodetectors and optical waveguide devices.[1] These compounds have advantages that include low-cost, flexibility and bio-compatibility.[2]

There is a plethora of organic molecules that have been used as organic semiconductors, including polymers and oligomers with donor–acceptor (D–A) architectures, that consist of an electron donor (D) and an electron acceptor (A) connected by a π-conjugated bridge, which facilitates intramolecular charge transfer (ICT).[3] In these compounds, modifying their electronic structures with the aim of developing low-band gap semiconductors with high charge-carrier mobilities is feasible. Variation of the HOMO and LUMO energy values through the introduction of different donor and acceptor groups is the best strategy to tune the electronic and optoelectronic properties of these systems for device applications. Given the variety of chemical synthesis methods, the organic semiconducting materials can be modified to fulfill the demands of different applications.[4]

However, the performance of organic semiconductors is governed not only by the molecular structure but also by how molecules or polymer chains assemble in the solid state.[5] Intermolecular interactions such as hydrogen bonding, π–π stacking and electrostatic forces can be used to tune the factors that influence the self-assembly and the final morphologies of the aggregates. Compared with thin films, one-dimensional (1D) organic semiconductors, due to their confined sizes and unique shapes, have proven to exhibit novel properties.[6,7] Furthermore, the more ordered packing structures in 1D crystalline organic semiconductors lead to relatively better and more reproducible device performance.[8] On the other hand, 1D organic semiconductors have fewer grain boundaries and defects and this gives rise to better charge-carrier transport properties. An understanding of structure-property relationships is therefore an important goal.

Among all the electronic devices, organic field effect transistors (OFETs) have attracted enormous interest.[9] These devices consist of an organic semiconducting layer, a gate insulator layer, and three terminals (source, drain and gate electrodes). OFETs are essential building blocks for the next generation of cheap and flexible organic circuits. However, they also provide an important insight into the charge transport of π-conjugated systems.[10] Therefore, OFETs have been the focus of attention for numerous researchers in the last two decades because of their enormous potential as fundamental elements in electronic devices, such as electronic papers,[11] displays,[12] radio frequency identification (RFID) tags, and sensors.[13]

In addition to this, multifunctionality is greatly desirable in materials science. In this sense, the appropriate choice of substituents allows control not only of the structure of the

[a]*Department of Organic Chemistry, Faculty of Chemical and Technologies Sciences, University of Castilla La Mancha-IRICA, 13071 Ciudad Real, Spain. E-mail: MariaPilar.Prieto@uclm.es; Ivan.TorresMoya@uclm.es*

[b]*Department of Physical Chemistry, Faculty of Sciences, University of Málaga, 29071 Málaga, Spain. E-mail: rocioponce@uma.es*

† Electronic supplementary information (ESI) available. See DOI: 10.1039/c8ra03246g

Open Access Article. Published on 13 June 2018. Downloaded on 12/9/2025 11:10:54 AM.
This article is licensed under a Creative Commons Attribution-NonCommercial 3.0 Unported Licence.

material but also of its properties. Thus, appropriate control of the starting molecular components enables the formation of supramolecular nanoscopic architectures that combine several properties and have a range of potential applications.[14,15]

In this respect, the 2*H*-benzo[*d*][1,2,3]triazole ring is an electron-deficient system that plays an important role as an acceptor moiety. This unit can be easily modified by alkylation at the central nitrogen and the introduction of different groups in the benzene ring, thus making it an excellent unit with great applicability in different fields.[16]

Some of us previously described the self-assembly of 2*H*-benzo[*d*][1,2,3]triazole derivatives to afford ribbons exhibiting an optical waveguiding behavior.[17,18] In an effort to highlight the multifunctionality of these compounds, in this paper we describe the characterization and application as organic field-effect transistors of ten 2*H*-benzo[*d*][1,2,3]triazole derivatives. The electronic and molecular structures of these organic semiconductors were analyzed by DFT calculations, Raman spectroscopy, AFM techniques, and XRD, amongst others. The electrical performance of the materials was tested in OFET devices and they showed potential as p-type semiconductors.

Results and discussion

In this work, the applicability of 2*H*-benzo[*d*][1,2,3]triazole (**Bzt-Ar**) derivatives (Scheme 1) as p-type semiconductors in OFETs has been evaluated in order to assess their multifunctionality. It is well known that molecules with highly planar backbones and widely delocalized π-conjugation usually show efficient supramolecular order, good charge mobility and therefore are promising candidates as semiconductor materials in organic electronics. In this sense, benzotriazole derivatives appear to be excellent moieties to achieve this goal, when functionalized with electron rich groups[19] with different electronic effects as described here.

As a first approach, with the aim of determining the possible applicability of these compounds as semiconductor layers in OFETs, different aspects related to molecular geometry and electronic properties have been studied theoretically and experimentally. Computational calculations constitute a powerful tool in order to elucidate the experimental data and to assess information on the mechanism of charge transport in organic materials. Furthermore, theoretical calculations can be used to predict molecular properties, thus supporting a rational design of new materials, avoiding unnecessary synthesis. In this work, theoretical DFT calculations of the studied organic semiconductors have been carried out at the B3LYP/6-31G(d,p) level in order to establish structure-property relationships.

(a) DFT-optimized geometries

DFT theoretical calculations on the 2-(3,5-bis(trifluoromethyl)phenyl)-2*H*-benzo[*d*][1,2,3]triazole derivatives indicate that the benzotriazole core and the arylalkynyl fragment are basically coplanar (Table S1†), which is desirable for achieving effective π-conjugation. However, the functionalization with different alkyl groups can have an impact on skeleton planarity. In fact,

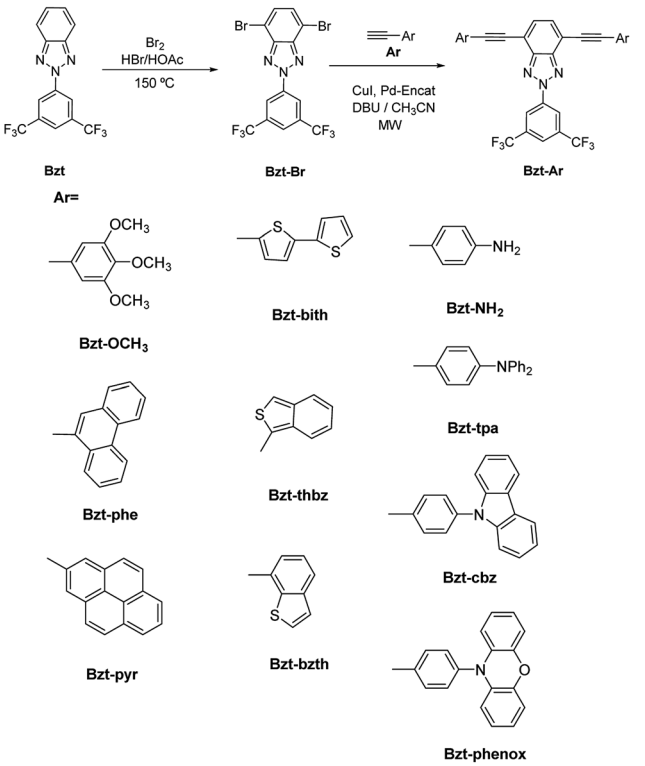

Scheme 1 Synthesis of 2-(3,5-bis(trifluoromethyl)phenyl)-4,7-bis(arylethynyl)-2*H*-benzo[*d*][1,2,3]triazole derivatives (**Bzt-Ar**) by a Sonogashira cross-coupling reaction between **Bzt-Br** and **Ar**.

a certain torsion angle between the benzotriazole core and the donor group is found for some of the studied semiconductors. For example, in **Bzt-phe** and **Bzt-pyr** the dihedral angle is close to 110° (Fig. 1a) due to steric hindrance between the hydrogen atoms of the phenanthrene (**Bzt-phe**) or pyrene (**Bzt-pyr**) units and the trifluoromethyl groups.

It is worth mentioning that in **Bzt-cbz** and **Bzt-phenox** the donor fragment is perpendicular to the central core, which could have a detrimental effect on their crystal packing and therefore on their electrical properties (Fig. 1b).

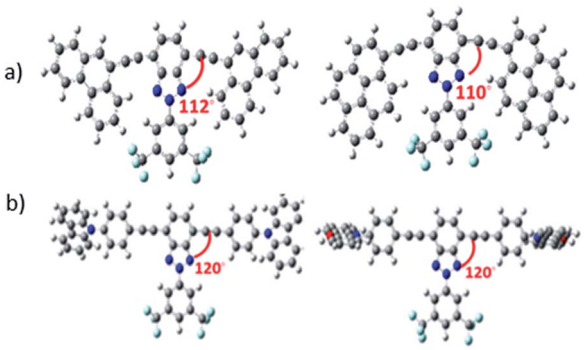

Fig. 1 Optimized structures calculated at the B3LYP/6-31G(d,p) level for the non-planar structures under study: (a) **Bzt-phe** and **Bzt-pyr** and (b) **Bzt-cbz** and **Bzt-phenox**. The dihedral angle between the benzotriazole core and the donor group is shown in red.

This journal is © The Royal Society of Chemistry 2018

Open Access Article. Published on 13 June 2018. Downloaded on 12/9/2025 11:10:54 AM.
This article is licensed under a Creative Commons Attribution-NonCommercial 3.0 Unported Licence.

(b) DFT-calculated molecular orbital energies and topologies and photophysical data

DFT calculations indicate similar frontier molecular orbital topologies for all derivatives. As an example, the topologies of the HOMO and LUMO orbitals of **Bzt-tpa** are depicted in Fig. 2. The HOMO orbital is located on the arylalkynyl fragment and the LUMO orbital in the benzotriazole core. Moreover there is an overlap between HOMO and LUMO orbitals, which indicates the intramolecular charge transfer character of the HOMO–LUMO transition.

Experimental optical absorption and photoluminescence spectra were recorded in order to determine the ICT character of the HOMO–LUMO transition and to quantify band gap energy values.

These spectra were recorded for diluted solutions of compounds **Bzt-Ar** in chloroform (Fig. 3, Fig. S1† and Table 1). It can be observed from the absorption spectra that all of these compounds show two bands, being the lowest energy one characteristic of intramolecular charge transfer (ICT),[20] and ascribed theoretically to a HOMO–LUMO transition. In addition, on the basis of these results, the optical band gaps were estimated from the onset of the lowest energy absorptions and were found to be in good agreement with the theoretical calculations (Table 1).

Moreover, the determination of HOMO and LUMO energy levels is feasible by cyclic voltammetry measurements. In this case these measures were performed on 1.5×10^{-4} M chloroform solutions of the compounds using 0.1 M tetrabutylammoniumhexafluorophosphate (NBu_4PF_6) as the supporting electrolyte (Table 2, Fig. 4 and S2–S10 in the ESI†). An Ag/AgCl electrode was used as the reference and potentials were referenced against the ferrocene/ferrocenium redox couple (0.1 V *vs.* SCE). From these data, the ionization potential (E_{HOMO}) and electron affinity (E_{LUMO}) values were estimated for the novel semiconductors. These values were calculated from the oxidation and reduction potential data by using standard approximations [eqn (1) and (2)], considering that the energy level of ferrocene/ferrocenium is 4.80 eV lower in vacuum.[21] The values obtained are listed in Table 2.

$$E_{HOMO} = -(E_{ox} + 4.80)\ (eV) \quad (1)$$

$$E_{LUMO} = -(E_{red} + 4.80)\ (eV) \quad (2)$$

It is worth noting that the E_{red} values are similar for all compounds indicating comparable LUMO energy levels. As indicated by the theoretical calculations, the LUMO is located on the benzotriazole core, which is common to all of the semiconductors, and thus the similar values. The major differences appear in the E_{ox} related to HOMO values, which is logic considering that HOMO orbitals are located on the donor groups, and those vary from molecule to molecule.

Therefore, the introduction of different substituents in the alkynyl fragment allows modulation of the semiconductor donor ability. By comparing donor groups containing a nitrogen atom it becomes clear that compounds where an electron pair is available (*i.e.* **Bzt-NH$_2$**, **Bzt-tpa** and **Bzt-phenox**) show enhanced

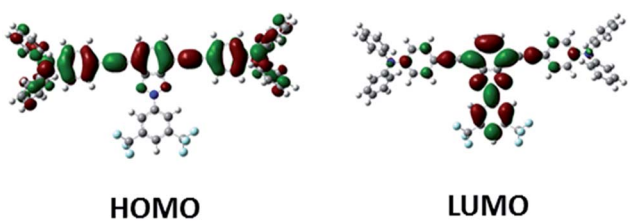

Fig. 2 HOMO and LUMO orbitals of **Bzt-tpa** calculated at the B3LYP/6-31G(d,p) level.

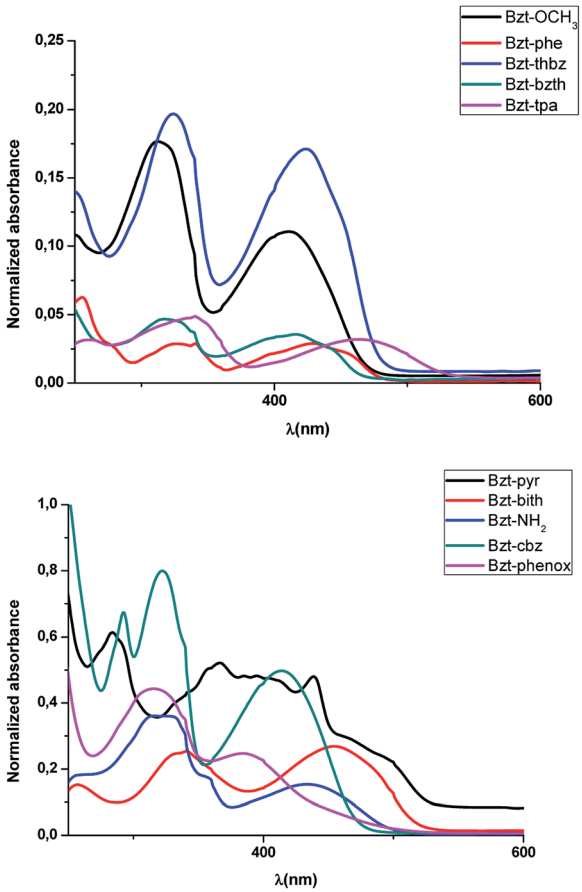

Fig. 3 UV/visible absorption spectra of compounds **Bzt-Ar** (298 K, $CHCl_3$, 1×10^{-5} M).

Table 1 Photophysical properties of **Bzt-Ar** derivatives. E_{gap} values in parentheses refer to B3LYP/6-31G(d,p) theoretical data

Compound	λ_{max} (nm)	ε (M^{-1} cm^{-1})	λ_{onset} (nm)	E_{gap} (eV)
Bzt-OCH$_3$	412	11 00 000	481	2.58 (2.81)
Bzt-phe	421	3 00 000	498	2.49 (2.64)
Bzt-pyr	439	17 00 000	540	2.30 (2.39)
Bzt-bith	455	8 00 000	536	2.31 (2.39)
Bzt-thbz	424	17 00 000	495	2.50 (2.27)
Bzt-bzth	411	4 00 000	476	2.60 (2.77)
Bzt-NH$_2$	434	6 00 000	506	2.45 (2.48)
Bzt-tpa	464	3 20 000	556	2.29 (2.39)
Bzt-cbz	414	45 00 000	480	2.58 (2.58)
Bzt-phenox	384	45 00 000	581	2.13 (1.89)

Open Access Article. Published on 13 June 2018. Downloaded on 12/9/2025 11:10:54 AM.
This article is licensed under a Creative Commons Attribution-NonCommercial 3.0 Unported Licence.

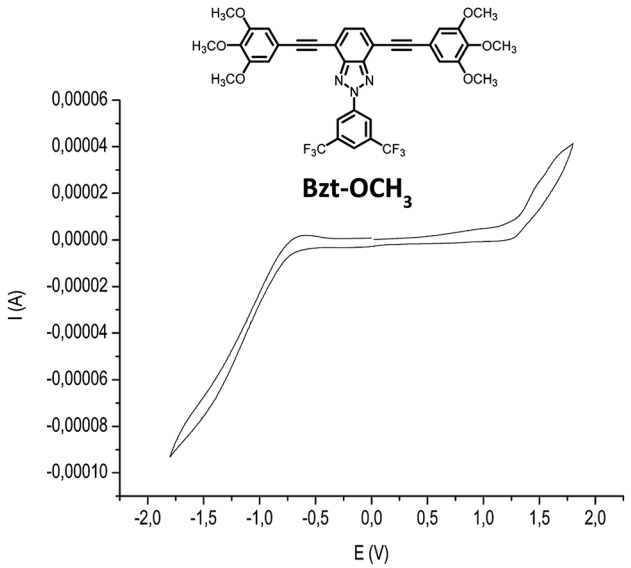

Fig. 4 Cyclic voltammograms of compound **Bzt-OCH$_3$**.

donor ability (Table 2, entries 7, 8 and 10). In contrast, compound **Bzt-cbz**, which does not have an available lone pair on the nitrogen because it takes part in the aromatic system, has the highest oxidation potential. In this sense, the results show superior donor ability of the nitrogen derivative (**Bzt-NH$_2$**) when compared to the oxygen derivative (**Bzt-OCH$_3$**) (Table 2, entries 7 and 1).

It should be pointed out that the redox processes are difficult in compounds with a thiophene moiety, such as **Bzt-bith** and **Bzt-bzth** (Table 2, entries 4 and 6). A plausible explanation is that delocalization of the charges into the electrogenerated radicals, which disrupts the aromaticity of the thiophene ring, requires a higher electron cost.

In all compounds, the HOMO values are close to the Fermi level of Au, indicating a potential flow of positive charge carriers between the HOMO orbital and the metal. For these reason, it could be expected that these BTz derivatives could behave as a p-type semiconductors.

Table 2 Electrochemical potentials and Frontier orbital values

Entry	Compound	E_{red}[a]	E_{ox}[a]	HOMO[b] (eV)	LUMO[b] (eV)
1	**Bzt-OCH$_3$**	−1.52	1.64	−6.07	−2.91
2	**Bzt-phe**	−1.56	1.61	−6.04	−2.87
3	**Bzt-pyr**	−1.48	1.59	−6.02	−2.95
4	**Bzt-bith**	−1.50	1.35	−5.78	−2.93
5	**Bzt-thbz**	−1.63	1.08	−5.51	−2.80
6	**Bzt-bzth**	−1.70	1.68	−6.11	−2.73
7	**Bzt-NH$_2$**	−1.52	0.99	−5.42	−2.91
8	**Bzt-tpa**	−1.26	1.30	−5.73	−3.17
9	**Bzt-cbz**	−1.36	1.50	−5.93	−3.07
10	**Bzt-phenox**	−1.69	0.98	−6.11	−2.74

[a] Electrochemical potentials *vs.* saturated calomel electrode (SCE) for compounds **Bzt-Ar** in $CHCl_3$. [b] Frontier orbital energies calculated from cyclic voltammetry data.

(c) DFT-caculated intramolecular reorganization energies

One fundamental theoretical parameter that can be related to charge transport is the intramolecular reorganization energy, which reflects the geometric changes needed to accommodate charge. Thus, lower reorganization energies normally are associated with more efficient charge transport. This parameter has been calculated as reported previously.[22] In particular, the intramolecular reorganization energy (λ) associated with an intermolecular charge transfer reaction consists of two terms related to the geometry relaxation energies upon going from the neutral state to a charged molecular state and *vice versa*, and it is given by the expression (eqn (3)):

$$\lambda = \lambda_{rel}^{(1)} + \lambda_{rel}^{(2)} \quad (3)$$

where $\lambda_{rel}^{(1)}$ and $\lambda_{rel}^{(2)}$ were computed directly from the adiabatic potential-energy surfaces as:

$$\lambda_{rel}^{(1)} = E^{(1)}(N) - E^{(0)}(N) \quad (4)$$

$$\lambda_{rel}^{(2)} = E^{(1)}(I) - E^{(0)}(I) \quad (5)$$

where $E^{(0)}(N)$ and $E^{(0)}(I)$ are the ground-state energy of the neutral and the radical cation molecular state, respectively; $E^{(1)}(N)$ is the energy of the neutral molecule at the optimal ion geometry, and $E^{(1)}(I)$ is the energy of the ionized state at the optimal geometry of the neutral molecule.

Following this procedure, λ calculated values at the B3LYP/6-31G(d,p) level for all compounds are shown in Table 3. As these compounds are expected to act as p-type semiconductors, the reorganization energies have only been calculated for hole transport.[23]

Moderate reorganization energies were predicted for all the compounds, with values in the range between 0.14 and 0.38 eV. These values are on the same order than other benchmark hole-transport materials, such as rubrene (0.16 eV)[24] or phenyl-substituted dithienoacene (0.31 eV).[25] Within the series, the compounds showing the highest values are **Bzt-OCH$_3$** and **Bzt-NH$_2$**, which can be related with the greater conformational freedom of the lateral substituents. Therefore, our results show that the easy one-electron reversible oxidation of our Donor–π–Acceptor–π–Donor systems together with their moderate

Table 3 Intramolecular reorganization energies (λ) for hole transfer computed at the B3LYP/6-31G(d,p) theory level for the studied **Bzt-Ar** derivatives

Compound	λ_h (eV)
Bzt-OCH$_3$	0.33
Bzt-phe	0.19
Bzt-pyr	0.14
Bzt-bith	0.16
Bzt-thbz	0.20
Bzt-bzth	0.18
Bzt-NH$_2$	0.38
Bzt-tpa	0.20
Bzt-cbz	0.14
Bzt-phenox	0.18

This journal is © The Royal Society of Chemistry 2018

Open Access Article. Published on 13 June 2018. Downloaded on 12/9/2025 11:10:54 AM.
This article is licensed under a Creative Commons Attribution-NonCommercial 3.0 Unported Licence.

predicted values of hole intramolecular reorganization energy would render them as potential hole-transport material candidates.

(d) Raman spectroscopy

FT-Raman spectra were also recorded in order to gather information on the degree of π-conjugation of the various semiconductors, as previously demonstrated for other types of organic materials.[26,27] More conjugated structures are desirable for efficient stabilization of the injected charge. Theoretical Raman spectra were obtained by DFT calculations and the results were compared with the experimental ones. The obtained results are collected in Table 4.

We will focus our discussion on the analysis of two characteristic bands: the vibration recorded at ~1470 cm^{-1} located on the benzotriazole group and the stretching vibration of the C≡C triple bond, at ~2200 cm^{-1}. No remarkable changes are recorded for the vibration at ~1470 cm^{-1}. In marked contrast, the ν(C≡C) is highly sensitive to the donor group variation. For this reason, this latter band is optimal to evaluate the effectiveness of the different semiconductors. Thus, a downshift of this Raman vibration indicates more effective π–π conjugation and therefore, improved intramolecular charge transfer.

As an example, a comparison between the experimental and theoretical Raman spectra for **Bzt-OCH$_3$** is shown in Fig. 5. Other spectra can be found in the ESI (Fig. S11–S19†).

Comparison of compounds with thiophene groups (**Bzt-bith**, **Bzt-thbz** and **Bzt-bzth**) shows displacements of the C≡C triple bond stretching due to the different degree of π-conjugation. In particular, the displacement of this vibration toward lower wavenumbers follows the trend: **Bzt-bzth** → **Bzt-thbz** → **Bzt-bith**, indicating that a thiophene ring linker between acceptor and donor groups is somewhat desirable for efficient π-conjugation. On the contrary, the more aromatic character of the benzene ring prevents efficient charge delocalization, diminishing intramolecular charge transfer.

In the cases of **Bzt-phe** and **Bzt-pyr**, where the donor group is a phenanthrene and a pyrene, respectively, it can be observed that the displacement is less marked in **Bzt-phe** than in **Bzt-pyr**. As a result, the π conjugation must be better in **Bzt-phe** despite the fact that the number of rings is lower than in **Bzt-pyr**. This

Table 4 Experimental Raman data for semiconductors Bzt-Ar. Values in parentheses refer to B3LYP/6-31G(d,p) theoretical data

Compound	Benzotriazole band (cm^{-1})	C≡C triple bond stretching (cm^{-1})
Bzt-OCH$_3$	1474 (1462)	2202 (2300)
Bzt-phe	1474 (1460)	2197 (2287)
Bzt-pyr	1476 (1460)	2207 (2277)
Bzt-bith	1473 (1459)	2187 (2272)
Bzt-thbz	1472 (1456)	2193 (2259)
Bzt-bzth	1472 (1461)	2200 (2295)
Bzt-NH$_2$	1473 (1461)	2204 (2291)
Bzt-tpa	1475 (1461)	2198 (2289)
Bzt-cbz	1474 (1461)	2193 (2296)
Bzt-phenox	1472 (1461)	2210 (2300)

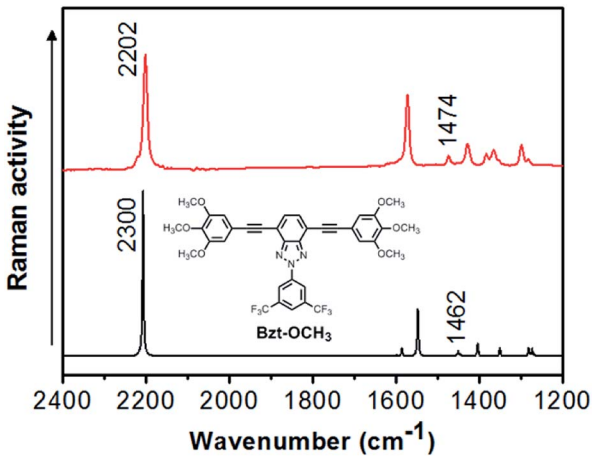

Fig. 5 Comparison between experimental Raman spectra (red) and theoretical Raman spectra (black) for Bzt-OCH$_3$. Theoretical spectra were calculated at the B3LYP/6-31G(d,p) theory level.

situation is similar to the previous case. In **Bzt-pyr**, in contrast to the expected behaviour, the higher number of benzene rings improves the charge delocalization in the structure but makes the internal charge transfer between the donor and acceptor group more difficult, this effect increasing with the number of rings.

Finally, donor groups that contain nitrogen atoms, such as in **Bzt-NH$_2$**, **Bzt-tpa**, **Bzt-cbz** and **Bzt-phenox**, were compared. The compounds **Bzt-tpa**, **Bzt-cbz** and **Bzt-phenox** contain a large number of benzene rings and, for this reason, aromatization must be higher than in **Bzt-NH$_2$**, which contains only one aniline group. However, the ν(C≡C) vibration appears at higher wavenumber in **Bzt-phenox** than in **Bzt-NH$_2$**. The phenylphenoxazine group is highly electron-withdrawing and therefore attracts the charge strongly, thus leading to worse delocalisation than in the other cases. On the other hand, the difference between **Bzt-tpa** and **Bzt-cbz** can be related to structural parameters. Note that while the triphenylamine group is not planar the phenylcarbazole is indeed planar, improving the π-conjugation and charge delocalisation which is supported by the downshift of the ν(C≡C) band.

In general, there is a good agreement between theoretical and experimental results. Bearing in mind the Raman spectroscopy results, the HOMO energy levels, the reorganization energy values and the geometry calculated, it can be expected **Bzt-phe**, **Bzt-bith**, **Bzt-bzth**, **Bzt-tpa** and **Btz-cbz** to be the best candidates as semiconductors in OFETs. However, note that other supramolecular parameters, such as molecular ordering within the thin film are crucial in the charge transport process, and may control the device performance.

(e) Electrical characterization

The charge-transport properties of the benzotriazole derivatives and their behaviour as organic semiconductors were evaluated by fabricating top-contact/bottom-gate field-effect transistors by organic semiconductor vapour deposition in vacuum on Si/SiO_2 substrates treated with octadecyltrichlorosilane (OTS) or

Open Access Article. Published on 13 June 2018. Downloaded on 12/9/2025 11:10:54 AM.
This article is licensed under a Creative Commons Attribution-NonCommercial 3.0 Unported Licence.

hexamethyldisilazane (HMDS), followed by thermal gold deposition using shadow masks to define the source and drain electrodes. The parameters required to define the properties and behaviour as an OFET can be extracted from the *I–V* response plots in the saturation regime by using the assumptions of conventional transistor formalisms [eqn (6)]. The efficiency of OFETs can be determined by the drain current in the saturation regime ((I_D)sat) [eqn (6)], where W is the channel width, L the channel length, C the capacitance per unit area or the insulator layer and V_G the gate voltage. The calculated parameters are field-effect mobility (μ), I_{ON}/I_{OFF} ratio and threshold voltage (V_T).[28,29]

$$(I_D)_{sat} = (W/2L)\mu C(V_G - V_T)^2 \quad (6)$$

The OFET parameter data for films of **Bzt-Ar** are summarized in Table 5. It should be pointed out that these results correspond to HMDS-treated Si/SiO_2 substrates as these provided better electrical figures. To calculate these parameters, transfer plots of $(I_D)_{sat}$ *vs.* V_G were used to determine the saturation mobility, I_{ON}/I_{OFF} ratio and threshold voltage for the different fabricated devices. The parameters were calculated with V_D = 100 V for hole transport. Some representative output and transfer plots for **Bzt-tpa** are shown in Fig. 6.

The results summarized in Table 5 indicate that seven of the studied compounds showed charge transport at negative biases indicating their potential as p-type semiconductors. The results are consistent with the values for the HOMO and LUMO frontier orbitals. All of the HOMO values are around −5.0 eV, *i.e.*, close to the Fermi level of the electrode (gold), but the LUMO levels are far from this latter.

The hole mobilities (λ_h) are modest, in the range 10^{-4} to 10^{-5} $cm^2\ V^{-1}\ s^{-1}$. Note that a certain dependence with mobility and the donor group used can be found.

In general, the mobility values are in good agreement with the π-conjugation degree derived from the C≡C triple bond stretching frequencies recorded by Raman spectroscopy, indicating that lower ring aromaticity lead to improved charge delocalisation in the structure. Thus, the injected charges are expected to be more easily stabilized for the less aromatic compounds. As a consequence, compound **Bzt-thbz** having a lower ν(C≡C) frequency is a more efficient semiconductor than **Bzt-bzth**. Finally, **Bzt-phe** and **Bzt-pyr** show similar behaviour. However, in this case it can be seen from the optimized structure found by DFT calculations that there is another explanation for this behaviour. In both cases there is a torsion angle between the donor and acceptor groups and this becomes more marked as the number of benzene rings increases (Fig. 2). As a consequence, in **Bzt-pyr** there is significant torsion that prevents molecular orbital overlapping between neighbour molecules and thus intermolecular charge transport is hindered as a consequence.

Table 5 OFET electrical data for devices fabricated with organic semiconductors **Bzt-Ar** measured in vacuum

Semiconductor (HMDS 90 °C)	μ_h ($cm^2\ V^{-1}\ s^{-1}$)	V_T (V)	I_{ON}/I_{OFF}
Bzt-phe	2.69×10^{-4}	−57	2×10^3
Bzt-pyr	3.31×10^{-5}	−40	1×10^2
Bzt-thbz	1.80×10^{-4}	−69	8×10^3
Bzt-bzth	3.76×10^{-5}	−13	4×10^2
Bzt-tpa	1.21×10^{-4}	−38	2×10^2
Bzt-cbz	2.02×10^{-5}	−58	3×10^2
Bzt-phenox	2.04×10^{-5}	−40	5×10^2

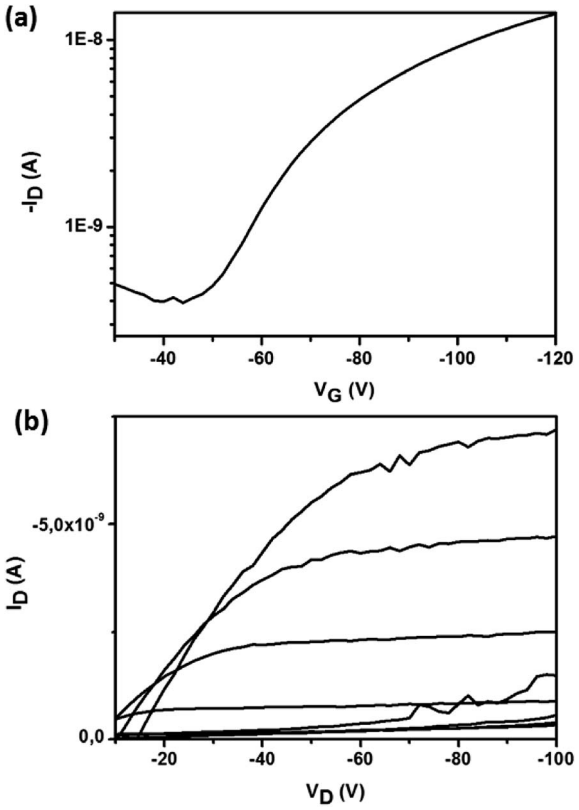

Fig. 6 (a) Transfer (at a fixed V_D value of 100 V) and (b) output plots (V_G was varied from 20 V to −120 V) for compound **Bzt-tpa** for hole transport.

In an effort to explain the results, the characteristics of thin films were studied by techniques such as wide-angle X-ray diffraction (WAXRD) and atomic force microscopy (AFM). These two techniques provide information about microstructural regularity and allow a good estimation of the molecular orientation with respect to the gate insulator surface. It is known that the best orientation between the source and drain electrodes occurs when the cofacial π-conjugated molecular planes are aligned perpendicular to the dielectric substrate surface, thus increasing charge transport.[30] For this purpose, only vapour-deposited films on preheated (90 °C) HMDS-treated Si/SiO_2 substrates were studied.

Comparison of the XRD results for **Bzt-tpa**, **Bzt-cbz** and **Bzt-phenox** (Fig. 7) shows that they are consistent with the OFET parameters. Two peaks can be observed for **Bzt-tpa**, indicating a polycrystalline film. In contrast, **Bzt-cbz** and **Bzt-phenox** were essentially amorphous since Bragg reflections were not detected. A plausible explanation for this finding lies in the fact that the phenylcarbazole and phenylphenoxazine groups are planar

 This journal is © The Royal Society of Chemistry 2018

Open Access Article. Published on 13 June 2018. Downloaded on 12/9/2025 11:10:54 AM.
This article is licensed under a Creative Commons Attribution-NonCommercial 3.0 Unported Licence.

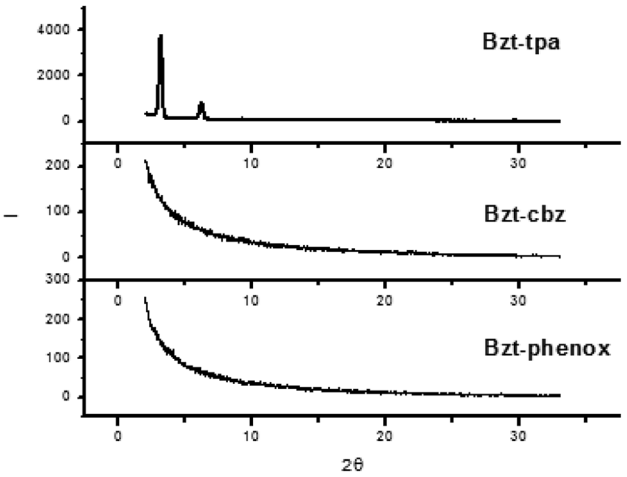

Fig. 7 X-ray diffraction scans of vapour-deposited **Bzt-tpa**, **Bzt-cbz** and **Bzt-phenox** at 90 °C on substrates treated with hexamethyldisilazane (HMDS).

but they are perpendicular to the benzotriazole core, thus distorting the planarity and hindering the appropriate self-assembly. As a result, the structures of **Bzt-cbz** and **Bzt-phenox** are less crystalline than that of **Bzt-tpa**, despite its non-planar structure, but the orientation of the benzene rings allows effective self-assembly through π–π stacking.

The XRD patterns for **Bzt-thbz** and **Bzt-bzth**, both including a thiophene ring in their molecular structures, are depicted in Fig. 8. The peak that appears at around 20 degrees is a key factor because it indicates efficient π–π stacking between molecular planes. This peak is only observed in **Bzt-thbz** but not in **Bzt-bzth**, which indicates a lower level of crystallinity in the latter. It is important to note the differences observed in samples at 90 °C and at room temperature in the case of **Bzt-bzth**. In

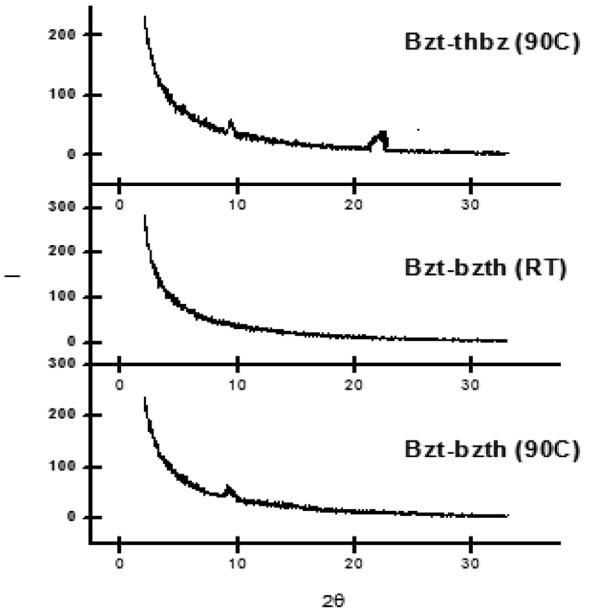

Fig. 8 X-ray diffraction scans of vapour-deposited **Bzt-thbz** and **Bzt-bzth** (room temperature and 90 °C) on substrates treated with hexamethyldisilazane (HMDS).

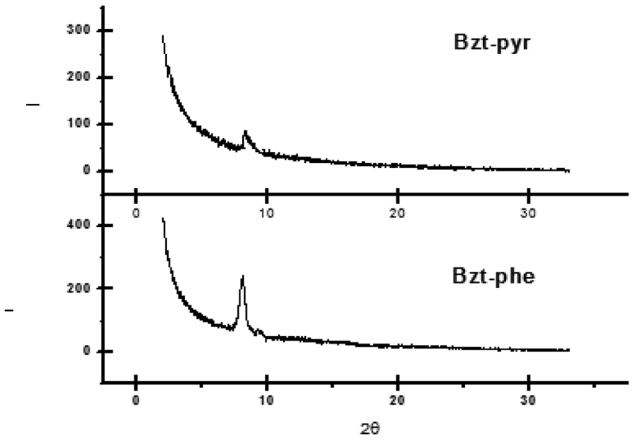

Fig. 9 X-ray diffraction scans of vapour-deposited **Bzt-phe** and **Bzt-pyr** (90 °C) on substrates treated with hexamethyldisilazane (HMDS).

general, it is known that higher temperatures provide better organization of the molecules in the active region, which may improve charge transport within the semiconductor layer. For this reason, an additional peak was observed in the sample at 90 °C when compared with the room temperature sample.

On comparing the XRD data for **Bzt-pyr** and **Bzt-phe** (Fig. 9) a high intensity peak is observed at around 8 degrees for **Bzt-phe** being this less intense in the case of **Bzt-pyr**, which indicates that the crystallinity is enhanced in the former. The high level of torsion in **Bzt-pyr** when compared to **Bzt-phe** in the optimized structure is another explanation for this finding as this torsion may hinder intermolecular crystal packing.

Thin films were also characterized by tapping mode AFM. The most crucial interface in a field-effect transistor is the dielectric–semiconductor interface, where charge transport takes place. Although that interface is buried, AFM imaging is often used to correlate film microstructures with charge transport. The morphologies of the vapour-deposited **Bzt-phe**, **Bzt-thbz** and **Bzt-tpa**, which are the compounds rendering the best mobilities, are in a good agreement with the XRD data. In all cases organized aggregates with well-defined fibres were

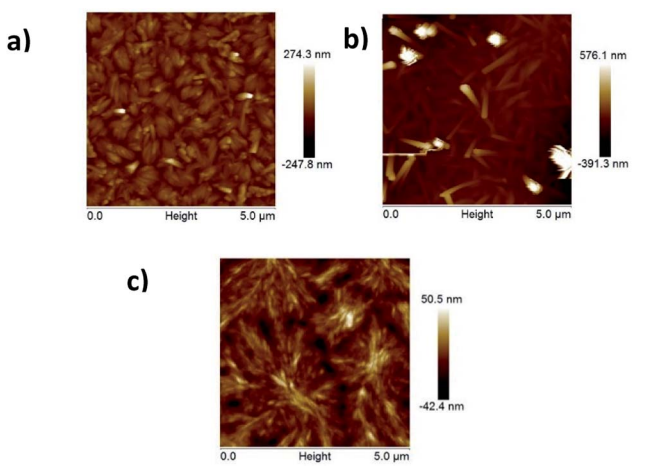

Fig. 10 AFM images of **Bzt-phe** HMDS 90 °C (a) **Bzt-thbz** HMDS 90 °C (b) **Bzt-tpa** HMDS 90 °C (c). Image size: 5 × 5 μm.

Open Access Article. Published on 13 June 2018. Downloaded on 12/9/2025 11:10:54 AM.
This article is licensed under a Creative Commons Attribution-NonCommercial 3.0 Unported Licence.

obtained, and this fact directly influences the electrical behaviour (Fig. 10).

In summary, all of the techniques employed in this study (DFT calculations, Raman spectroscopy, XRD and AFM) allow the establishment of useful relationships between the semiconductor electronic and molecular structures and the properties as organic semiconductors in OFETs for the different 2*H*-benzo[*d*][1,2,3]triazole derivatives.

Conclusions

In the present work, 4,7-bis(arylethynyl)-2*H*-benzo[*d*][1,2,3]triazole derivatives (**Bzt-Ar**) were tested as semiconductors in OFETs. The electronic and molecular structures of the semiconductors were tuned by maintaining the same central acceptor group, namely a benzotriazole with two trifluoromethyl groups to increase its acceptor ability, and including different donor groups. A total of ten different donor groups with varying electron donating strengths were evaluated.

The organic semiconductors were characterized by DFT calculations, X-ray diffraction, AFM, and FT-Raman spectroscopy. Analysis of the data obtained by the optical and vibrational techniques indicate that molecular planarity and efficient intramolecular charge transfer between acceptor and donor groups have an impact on their electrical properties.

Although the mobility values obtained here are modest, with values around 10^{-4} cm^2 V^{-1} s^{-1}, this study demonstrates for the first time the applicability of benzotriazole derivatives in organic electronics. Future modifications of these derivatives could improve their mobility and their applicability. Due to an adequate alignment between the energy levels of the semiconductors and the used electrodes, all of the semiconductors studied here act as p-type materials. The obtained results indicate that compounds **Bzt-phe**, **Bzt-thbz** and **Bzt-tpa** are the most promising candidates as organic semiconductors.

Finally, it is worth noting the multifunctionality of 2*H*-benzo[*d*][1,2,3]triazole derivatives, both as waveguide materials, which was previously described, and as p-type semiconductors in OFETs.

Experimental section

All reagents were used as purchased. Reactions with air-sensitive materials were carried out under an argon atmosphere. Flash chromatography was perfomed using silica gel (Merck, Kieselgel 60, 230–240 mesh or Scharlau 60, 230–240 mesh). Analytical thin layer chromatography (TLC) was performed using aluminium-coated Merck Kieselgel 60 F254 plates.

Cyclic voltammetry measurements were performed on a μ-Autolab ECO-Chemiepotentiostat using a glassy carbon working electrode, Pt counter electrode and Ag/AgCl reference electrode. The experiments were carried out under argon, in $CHCl_3$, with Bu_4NPF_6 as supporting electrolyte (0.1 mol L^{-1}). The scan rate was 50 mV s^{-1}.

UV-vis spectra were recorded on a Varian Cary model 5000 UV-vis-NIR spectrophotometer using standard quartz cells of 1 cm width and solvents of spectroscopic grade.

Theoretical calculations were carried out in the framework of density functional theory (DFT) using the B3LYP functional[31,32] and the 6-31G(d,p) basis set[33,34] as implemented in the Gaussian 09 programme.[35] Geometry optimizations were performed using the medium-sized 6-31G(d,p) basis set and frequency calculations were performed to confirm the nature of ground state stationary points. The reorganization energies were calculated through the relevant points on the potential energy surfaces.[36,37] Ground state redox potentials were calculated from the difference in Gibbs free energy between neutral molecules and oxidized radical ions in solutions using the CPCM solvation model.[38]

FT-Raman spectra with 1064 nm excitation were recorded using an FT Raman accessory kit (RamII) on a Bruker Vertex 70 FT-IR interferometer and a continuous-wave Nd:YAG laser. A germanium detector operating at liquid-nitrogen temperature was used and the Raman scattering radiation was collected in a back-scattering configuration with a 4 cm^{-1} spectral resolution. An average of 1000 scans were used in the reported spectra.

All top-contact/bottom-gate OFETs were fabricated with the benzotriazole derivatives **Bzt-Ar** as the active layer. Gate dielectrics (p-doped Si wafers with 300 nm thermally grown SiO_2 layers) were functionalized either with a hexamethyldisilazane (HMDS) or octadecyltrichlorsilane (OTS) self-assembled monolayer. The capacitance of the 300 nm SiO_2 gate insulator was 10 nF cm^{-2}. Prior to surface functionalization, the wafers were cleaned by immersing them twice for 30 seconds each in EtOH with sonication, drying with a stream of N_2 and treating with UV-ozone for 10 min. The cleaned silicon wafers were treated with hexamethyldisilazane (HMDS) by exposing them to HMDS vapour at room temperature in a closed air-free container under argon for a week, or were treated with octadecyltrichlorosilane (OTS) by immersion in a 3.0 mM humidity-exposed solution of OTS in hexane for 1 hour following a previously reported procedure.[39] Following OTS deposition, the substrates were sonicated with hexane, acetone, and finally with ethanol, and dried with an N_2 stream. The semiconductors were then vapour-deposited on preheated substrates.

After semiconductor deposition, the films were analysed by AFM and XRD techniques. X-ray diffraction patterns were recorded on a Bruker D8 Discover A25 diffractometer by employing a scanning range of $2\theta = 2$–33° with CuKα1 X-ray radiation. AFM images were registered in tapping mode on an atomic force microscope (Veeco Instruments Multi-ModeNanoscope V). OFET devices were completed by vapour deposition of gold electrodes through a shadow mask to define devices with various channel lengths and channel widths. Devices were characterized under vacuum and ambient conditions in an EB-4 Everbeing probe station with a 4200-SCS/C Keithley semiconductor characterization system.

Conflicts of interest

There are no conflicts to declare.

 This journal is © The Royal Society of Chemistry 2018

Open Access Article. Published on 13 June 2018. Downloaded on 12/9/2025 11:10:54 AM.
This article is licensed under a Creative Commons Attribution-NonCommercial 3.0 Unported Licence.

Acknowledgements

This work was financially supported by MINECO of Spain (project CTQ2014-53600-R and CTQ2015-66897-P) and UCLM (GI20163531). I. Torres is indebted to MEC for an FPU studentship. I. Arrechea acknowledges MINECO of Spain for a FPI fellowship. Technical support from the High Performance Computing Service of the University of Castilla-La Mancha and the Vibrational Spectroscopy Laboratory at Research Support Central Services (SCAI) at the University of Málaga are gratefully acknowledged.

Notes and references

1 (*a*) Q. Tang, L. Jiang, Y. Tong, H. Li, Y. Liu, Z. Wang, W. Hu, Y. Liu and D. Zhu, *Adv. Mater.*, 2008, **20**, 2947–2951; (*b*) T. Lei and J. Pei, *J. Mater. Chem.*, 2012, **22**, 785–798; (*c*) Y. Zhou, L. Wang, J. Wang, J. Pei and Y. Cao, *Adv. Mater.*, 2008, **20**, 3745–3749; (*d*) Y. Yao, H. Dong and W. Hu, *Adv. Mater.*, 2016, **28**, 4513–4523; (*e*) Q. Tai and F. Yan, *Adv. Mater.*, 2017, **29**, 1700192.

2 (*a*) B. A. D. Neto, P. H. P. R. Carvalho and J. R. Correa, *Acc. Chem. Res.*, 2015, **48**, 1560–1569; (*b*) T. Someya, Z. Bao and G. G. Malliaras, *Nature*, 2016, **540**, 379–385; (*c*) D. Chen and Q. Pei, *Chem. Rev.*, 2017, **117**, 11239–11268; (*d*) C. García-Astrain, C. Chen, M. Burón, T. Palomares, A. Eceiza, L. Fruk, M. A. Corcuera and N. Gabilondo, *Biomacromolecules*, 2015, **14**, 1302–1310.

3 Y. Wu and W. Zhu, *Chem. Soc. Rev.*, 2013, **42**, 2039–2058.

4 C. Wang, H. Dong, V. Hu, Y. Liu and D. Zhu, *Chem. Rev.*, 2012, **112**, 2208–2267.

5 F. J. M. Hoeben, P. Jonkheijm, E. W. Meijer and A. P. H. Schenning, *Chem. Rev.*, 2005, **105**, 1491–1546.

6 F. S. Kim, G. Ren and S. A. Jenekhe, *Chem. Mater.*, 2011, **23**, 682–732.

7 A. L. Briseno, S. C. B. Mannsfeld, S. A. Jenekhe, Z. Bao and Y. Xia, *Mater. Today*, 2008, **11**, 38–47.

8 L. Jiang, H. Dong and W. J. Hu, *Mater. Chem.*, 2010, **20**, 4994–5007.

9 (*a*) Y. Zhou, W. Liu, Y. Ma, H. Wang, L. Qi, Y. Cao, J. Wang and J. Pei, *J. Am. Chem. Soc.*, 2007, **129**, 12386–12387; (*b*) A. L. Briseno, S. C. B. Mannsfeld, C. Reese, J. Hancook, Y. Xiong, S. A. Jenekhe, Z. Bao and Y. Xia, *Nano Lett.*, 2007, **7**, 2847–2853; (*c*) L. Jiang, Y. Fu, H. Li and W. Hu, *J. Am. Chem. Soc.*, 2008, **130**, 3937–3941; (*d*) J. Yang, D. Yan and T. S. Jones, *Chem. Rev.*, 2015, **115**, 5570–5603.

10 (*a*) W. Huang, B. Yang, J. Sun, B. Liu, J. Yang, Y. Zou, J. Xiiong, C. Zhou and Y. Gao, *Org. Electron.*, 2014, **15**, 1050–1055; (*b*) Y. Huang, J. Sun, J. Zhang, S. Wang, H. Huang, J. Zhang, D. Yan, Y. Gao and J. Yang, *Org. Electron.*, 2016, **36**, 73–81.

11 J. A. Rogers, Z. Bao, K. Baldwin, B. Dodabalapur, V. Crone, R. Raju, V. Kuck, H. Katz, J. Amundson, J. Ewing and P. Drzaic, *Proc. Natl. Acad. Sci. U. S. A.*, 2001, **98**, 4835–4840.

12 G. Gelinck, P. Heremans, K. Nomoto and T. D. Anthopoulos, *Adv. Mater.*, 2010, **22**, 3778–3798.

13 Y. Guo, G. Yu and Y. Liu, *Adv. Mater.*, 2010, **22**, 4427–4447.

14 C. Reese and Z. Bao, *Mater. Today*, 2007, **10**, 20–27.

15 T. Hasegawa and J. Takeya, *Sci. Technol. Adv. Mater.*, 2009, **10**, 024314.

16 (*a*) D. Patel, F. Fude, Y. Ohnishi, K. Abboud, S. H. Hirata, K. S. Schanze and J. R. Reynolds, *J. Am. Chem. Soc.*, 2012, **134**, 2599–2612; (*b*) B. Liu, S. Ye, Y. Zou, B. Peng, Y. He and H. Zhou, *Chem. Phys.*, 2011, **212**, 1439–1496; (*c*) Y. Dong, W. Cal, M. Wang, Q. Li, L. Yilg, F. Huang and Y. Cao, *Org. Electron.*, 2013, **14**, 2459–2467; (*d*) Y. Dong, W. Cai, X. Hu, C. Zhong, F. Huang and Y. Cao, *Polymer*, 2012, **53**, 1465–1471.

17 I. Torres, J. R. Carrillo, A. Díaz-Ortiz, R. Martín, M. V. Gómez, L. Stegemann, C. A. Strassert, J. Orduna, J. Buendía, E. E. Greciano, J. S. Valera, E. Matesanz, L. Sánchez and P. Prieto, *RSC Adv.*, 2016, **6**, 36544–36553.

18 I. Torres, A. Díaz-Ortiz, L. Sánchez, J. Orduna, M. J. Blesa, J. R. Carrillo and P. Prieto, *Dyes Pigm.*, 2017, **142**, 212–225.

19 (*a*) Y. Liu, G. Xie, K. Wu, Z. Luo, T. Zhou, X. Zeng, J. Yu, S. Gong and C. Yang, *J. Mater. Chem. C*, 2016, **4**, 4402–4407; (*b*) C. Quinton, S. Thiery, O. Jeannin, D. Tondelier, B. Geffroy, E. Jacques, J. Rault-Berthelot and C. Poriel, *ACS Appl. Mater. Interfaces*, 2017, **9**, 6194–6206.

20 X. Lu, S. Fan, J. Wu, X. Jia, Z. S. Wang and G. Zhou, *Org. Lett.*, 2013, **15**, 3530–3533.

21 R. Ponce, H. Herrera, R. Blanco, H. Huang, A. Facchetti, T. J. Marks, Y. Zheng and J. L. Segura, *J. Am. Chem. Soc.*, **132**, 8440–8452.

22 M. C. Ruiz Delgado, E. G. Kim, D. A. da Silva and J. L. Bredas, *J. Am. Chem. Soc.*, 2010, **132**, 3375–3387.

23 (*a*) M. Y. Kuo, H. Y. Chen and I. Chao, *Chem.–Eur. J.*, 2007, **13**, 4750–4758; (*b*) O. Kwon, V. Coropceanu, N. E. Gruhn, J. C. Durivage, J. G. Laquindanum, H. G. Katz, J. Cornil and J. L. Brédas, *J. Chem. Phys.*, 2004, **120**, 8186–8194; (*c*) H. Y. Chen and I. Chao, *Chem. Phys. Lett.*, 2005, **401**, 539–545.

24 D. A. da Silva, E. G. Kim and J. L. Bredas, *Adv. Mater.*, 2005, **17**, 1072–1076.

25 Y. M. Sun, Y. Q. Ma, Y. Q. Liu, Y. Y. Liu, Y. Y. Lin, Z. Y. Wang, Y. Wang, C. A. Di, K. Xiao, X. M. Chen, W. F. Qiu, B. Zhang, G. Yu, W. P. Hu and D. B. Zhu, *Adv. Funct. Mater.*, 2006, **16**, 426–432.

26 R. Ponce, J. Casado, V. Hernández, J. T. López, P. Viruela, E. Ortí, K. Takimiya and T. Otsubo, *Angew. Chem., Int. Ed.*, 2007, **46**, 9057–9061.

27 G. Zerbi, M. Veronelli, S. Martina, A. D. Schlüter and G. Wegner, *Adv. Mater.*, 1994, **6**, 385–388.

28 S. M. Size and M. K. Lee. *Semiconductor devices: Physics and Technology*, Wiley, New York, 3 edn, 2012.

29 R. Ponce, A. Facchetti and T. J. Marks, *Chem. Rev.*, 2010, **110**, 205–239.

30 Y. Sun, Y. Liu and D. Zhu, *J. Mater. Chem.*, 2005, **15**, 53–65.

31 C. Lee, W. Yang and R. G. Parr, *Phys. Rev. B*, 1988, **37**, 785–789.

32 A. D. Becke, *J. Chem. Phys.*, 1993, **98**, 1372–1377.

33 P. C. Hariharan and J. A. Pople, *Theor. Chim. Acta*, 1973, **28**, 213–222.

Open Access Article. Published on 13 June 2018. Downloaded on 12/9/2025 11:10:54 AM.
This article is licensed under a Creative Commons Attribution-NonCommercial 3.0 Unported Licence.

34 W. J. Hehre, R. Ditchfield and J. A. Pople, *J. Chem. Phys.*, 1972, **56**, 2257–2261.

35 M. J. Frisch, G. W. Trucks, H. B. Schlegel, G. E. Scuseria, M. A. Robb, J. R. Cheeseman, G. Scalmani, V. Barone, B. Mennucci, G. A. Petersson, H. Nakatsuji, M. Caricato, X. Li, H. P. Hratchian, F. A. Izmaylov, J. Bloino, G. Zheng, J. L. Sonnenberg, M. Hada, M. Ehara, K. Toyota, R. Fukuda, J. Hasegawa, M. Ishida, T. Nakajima, Y. Honda, O. Kitao, H. Nakai, T. Vreven, J. A. Montgomery, J. E. Peralta, F. Ogliaro, M. Bearpark, J. J. Heyd, E. Brothers, K. N. Kudin, V. N. Staroverov, R. Kobayashi, J. Normand, K. Raghavachari, A. Rendell, J. C. Burant, S. S. Iyengar, S. J. Tomasi, M. Cossi, N. Rega, N. J. Millam, M. Klene, J. E. Knox, J. B. Cross, V. Bakken, C. Adamo, J. Jaramillo, R. Gomperts, R. E. Stratmann, O. Yazyev, A. J. Austin, R. Cammi, C. Pomelli, J. W. Ochterski, R. L. Martin, K. Morokuma, V. G. Zakrzewski, G. A. Voth, P. Salvador, J. J. Dannenberg, S. Dapprich, A. D. Daniels, O. Farkas, J. B. Foresman, J. V. Ortiz, J. Cioslowski and D. J. Fox, *Gaussian 09, Revision A.1*, Gaussian, Inc., Wallingford CT, 2009.

36 M. Malagoli and J. L. Brédas, *Chem. Phys. Lett.*, 2000, **327**, 13–17.

37 J. L. Brédas, D. Beljonne, V. Coropceanu and J. Cornil, *Chem. Rev.*, 2004, **104**, 4971–5004.

38 (*a*) A. Klamt and G. Schürmann, *J. Chem. Soc., Perkin Trans. 2*, 1993, 799–805; (*b*) J. Andzelm, C. Kölmel and A. Klamt, *J. Chem. Phys.*, 1995, **103**, 9312–9320; (*c*) V. Barone and M. Cossi, *J. Phys. Chem. A*, 1998, **102**, 1995–2001; (*d*) M. Cossi, N. Rega, G. Scalmani and V. J. Barone, *Comput. Chem.*, 2003, **24**, 669–681.

39 H. Li, F. S. Kim, G. Ren, E. C. Hollenbeck, S. Subramaniyan and S. A. Jenekhe, *Angew. Chem., Int. Ed.*, 2013, **52**, 5513–5517.

This journal is © The Royal Society of Chemistry 2018